Materials Science and Engineering A 375–377 (2004) 785–788

www.elsevier.com/locate/msea

Crystallization behavior of $(Fe_{100-x}Co_x)_{62}Nb_8B_{30}$ bulk amorphous alloy

M. Shapaan [a], J. Gubicza [a], J. Lendvai [a], L. K. Varga [b,*]

[a] *Department of General Physics, Eötvös University, P.O. Box 32, H-1518 Budapest, Hungary*
[b] *KFKI Research Institute for Solid state Physics and Optics, Hungarian Academy of Sciences, P.O. Box 49, H-1525 Budapest, Hungary*

Abstract

The effect of Co addition on the glass-forming ability (GFA) has been investigated in the $(Fe_{100-x}Co_x)_{62}$ Nb_8B_{30} ($x = 0$, 33, and 50) bulk amorphous alloy system by differential scanning calorimeter (DSC). The thermal stability measured by the apparent activation energies decreased from about 5.5 to 4.5 eV upon Co addition. The glass-forming ability measured by the temperature interval $T_x - T_g$ was decreased substantially compared to $Fe_{62}Nb_8B_{30}$ alloy, but it is still large enough for practical applications. The DSC and DTA parameters, T_g, T_x, T_m and T_l were combined in different parameters, T_g/T_m, T_x/T_l and $T_x/(T_g + T_l)$ and $T_x/(T_l - T_g)$ to express the glass-forming ability. The cystallization products were studied by XRD. The metastable $Fe_{23}B_6$ crystallization product was found in all the alloys.

Keywords: Bulk glass-forming ability; Differential thermal analysis; Crystallization

1. Introduction

Experimental works carried out by Itoi and Inoue [1] and Inoue [2] revealed that the increase of boron content from about 20% to 30 at % for Fe(Co,Ni)–Nb–B amorphous alloys caused an extension of the supercooled liquid region up to 80 K. The high boron content confers also high electrical resisitivity above 200 μΩ cm, which is very advantageous for high frequency applications of these soft magnetic alloys. While ribbon samples can be easily prepared by melt spinning with a fully amorphous structure, the critical thickness of bulk amorphous alloys depends strongly on the bulk glass-forming ability (BGFA). This property can be studied in terms of a number of parameters like reduced glass-transition temperature, T_g/T_m, reduced crystallization temperature, T_x/T_l or $T_x/(T_g + T_l)$ [3,4] and a new parameter $G = T_x/(T_l - T_g)$, where T_l is the offset temperature of melting and $T_l - T_g$ is the cooling increment [5]. The intention of this paper to present a comparative study of the BFGA for the $(Fe_{100-x}Co_x)_{62}Nb_8B_{30}$ alloys and to study the crystallization products after different crystallization steps.

2. Experimental procedure

Multi-component amorphous $(Fe_{100-x}Co_x)_{62}Nb_8B_{30}$ ($x = 33$ and 50) ribbons were prepared by melt spinning technique using Cu disk with tangential velocity of 25 m/s. The ribbon sample was about 35 μm thick and 4 mm wide. The amorphicity of the ribbons was examined by X-ray diffractometry (XRD). A Perkin-Elmer DSC-2 differential scanning calorimeter (DSC) was employed to determine the glass-transition temperature, crystallization temperature and crystallization enthalpy ΔH_x. All the calorimetric measurements were carried out in an argon flux in order to protect the sample against oxidation. The thermal transformation data above 1000 K were determined by DTA using SETARAM equipment. The structure of the as cast and heat treated ribbons were examined by X-ray diffractometry using a Bruker D8 advanced diffractometer with Cu radiation.

3. Results and discussion

Fig. 1a shows the X-ray diffraction pattern of the as cast $(Fe_{50}Co_{50})_{62}Nb_8B_{30}$ ribbon, indicating the formation of a mostly single amorphous phase. The wave vector ($K_p = 4\pi \sin\theta/\lambda$) at the maximum position of the main broad peak is measured as 30.85 nm^{-1}. Fig. 2 shows the DSC curves of

* Corresponding author. Fax: +36-1-3922220.
E-mail address: varga@szfki.hu (L.K. Varga).

0921-5093/$ – see front matter © 2003 Elsevier B.V. All rights reserved.
doi:10.1016/j.msea.2003.10.181

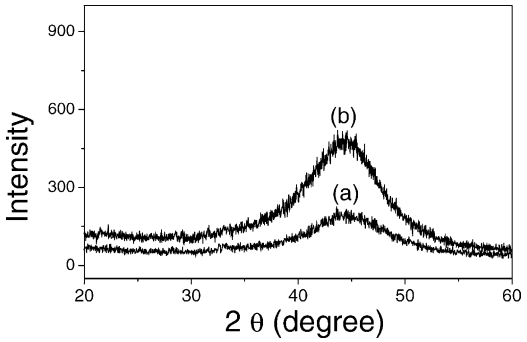

Fig. 1. X-ray diffraction patterns of $(Fe_{50}Co_{50})_{62}Nb_8B_{30}$ (a) as quenched ribbon and (b) heated up to 900 K (around the T_g) at heating rate of 20 K/min.

the $(Fe_{67}Co_{33})_{62}Nb_8B_{30}$ amorphous ribbon at heating rates of 10 and 20 K/min and the inset shows the DTA curve at heating rate of 10 K/min. It is seen that the alloy crystallizes through a single stage accompanied by an exothermic heat, where, the crystallization enthalpy (ΔH_x) is proportional to the area defined by the exothermic peak in the DSC trace. In addition to the exothermic peak, one can notice an endothermic reaction with a wide supercooled liquid region in the temperature range between the onset temperature of crystallization (T_x) and the glass-transition temperature (T_g). With increasing heating rate the glass-transition temperature and the crystallization temperature are shifted to higher temperatures in such a way that the difference $\Delta T_x = T_x - T_g$ is also increasing, in accordance with other literature data [6]. The effect of partial replacement of Fe by Co atoms on the glass-forming ability (GFA) we can see in Fig. 3. For $x = 50$, the glass-transition temperature shifted to a lower temperature at the same time the crystallization temperature shifted to a higher temperature leading to a wider supercooled liquid region. The inset shows the DTA curve at heating rate of 10 K/min. The thermal transition data are collected in Table 1 for all the alloys.

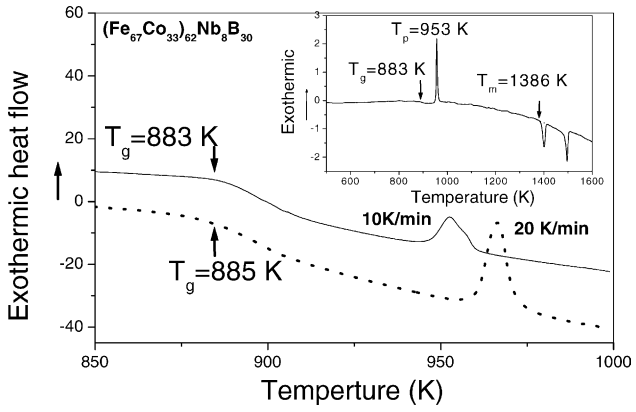

Fig. 2. DSC traces for $(Fe_{67}Co_{33})_{62}Nb_8B_{30}$ amorphous ribbon at heating rates of 10 and 20 K/min. The inset shows the DTA curve at heating rate of 10 K/min.

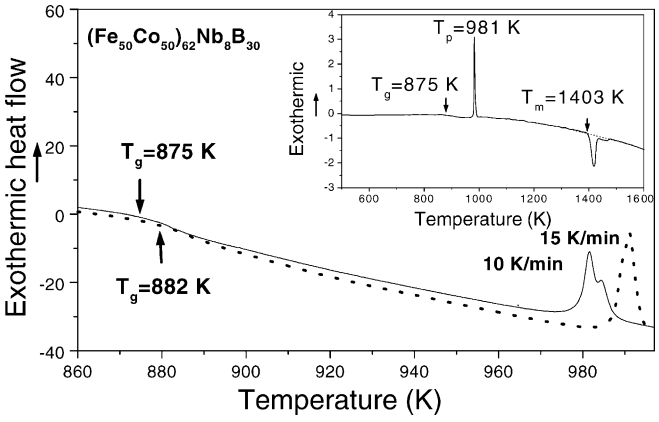

Fig. 3. DSC traces for $(Fe_{50}Co_{50})_{62}Nb_8B_{30}$ amorphous ribbon at heating rates of 10 and 15 K/min. The inset shows the DTA curve at heating rate of 10 K/min.

Fig. 1b. shows X-ray diffraction pattern of $(Fe_{50}Co_{50})_{62}NB_8B_{30}$ heated (heating rate: 20 K/min) up to 900 K, slightly above T_g. The pattern exhibits the same broad symmetric halo, which is typical of a fully amorphous phase, indicating that the material remained amorphous after this short heat treatment around T_g.

The apparent activation energy, the frequency factor and the rate constant of the crystallization are estimated using the Kissinger method [7,8]. The dependence of T_p on the heating rate β is described in this model by

$$\frac{\beta}{T_p^2} = \left(\frac{Z_{cr} R_g}{E_a}\right) \exp\left(-\frac{E_a}{R_g T_p}\right) \quad (1)$$

where Z_{cr} is the frequency factor, R_g the gas constant, and E_a the activation energy. Plotting $\ln(\beta/T_p^2)$ as a function of $1/T_p$ enables the calculation of E_a from the slope of this plot E_a/R_g and frequency factor Z_{cr} can be determined from the intercept of this line with the ordinate. The Kissinger plots data are collected in the Table 2 together with the parameters of the bulk glass-forming ability.

The temperature dependence of the crystallization rate constant K_{cr} determine from the Arrhenius law

$$K_{cr}(T) = Z_{cr} \exp\left(-\frac{E_a}{R_g T}\right) \quad (2)$$

Fig. 4 shows the Kissinger plots for $(Fe_{100-x}Co_x)_{62}Nb_8B_{30}$ ($x = 33$ and 50) and the inset shows the variation of K_{cr} with temperature. As the rate constant of the crystallization comprises all the relevant data of the crystallization (Z_{cr}, E_a

Table 1
Summary of DTA and DSC data T_g, T_x, ΔT_x, T_p, T_m and T_l at heating rate of 10 K/min of bulk amorphous $(Fe_{100-x}Co_x)_{62}Nb_8B_{30}$ alloys

Amorphous alloys	T_g (K)	T_x (K)	ΔT_x (K)	T_p (K)	T_m (K)	T_l (K)
$Fe_{62}Nb_8B_{30}$	897 ± 2	974	77	980	1403	1543
$(Fe_{67}Co_{33})_{62}Nb_8B_{30}$	883 ± 1	951	68	953	1386	1508
$(Fe_{50}Co_{50})_{62}Nb_8B_{30}$	875 ± 1	977	102	981	1403	1480

Table 2
Summary of thermal transition data and the parameters for BGFA of $(Fe_{100-x}Co_x)_{62}Nb_8B_{30}$ ($x = 0$, 33, and 50) alloys

Amorphous alloys	E_a (kJ/mol)	Z_{cr} (min^{-1})	ΔH_x (J/g)	T_g/T_m	$T_x/(T_g + T_l)$	$T_x/(T_l - T_g)$
$Fe_{62}Nb_8B_{30}$	541.7	7.8×10^{28}	81 ± 3	0.639	0.399	1.514
$(Fe_{67}Co_{33})_{62}Nb_8B_{30}$	404.8	11.4×10^{21}	95 ± 2	0.637	0.397	1.52
$(Fe_{50}Co_{50})_{62}Nb_8B_{30}$	457.5	12.7×10^{23}	97 ± 1	0.623	0.414	1.6

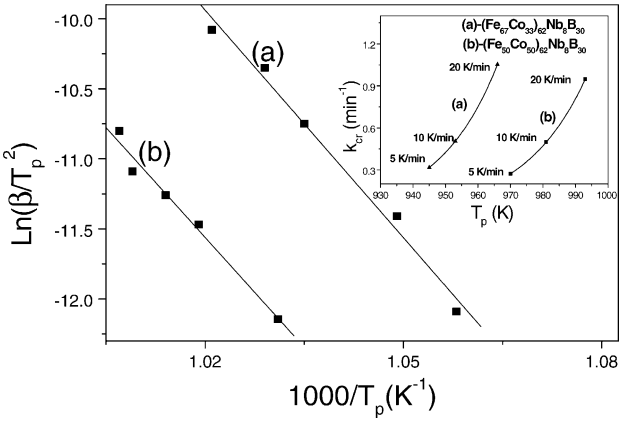

Fig. 4. Kissinger plots for $(Fe_{100-x}Co_x)_{62}Nb_8B_{30}$ ($x = 33$ and 50). The inset shows the temperature dependence of the crystallization rate constant K_{cr}.

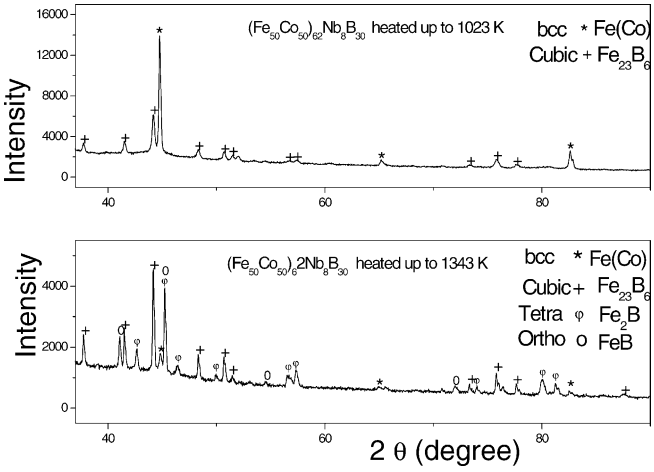

Fig. 6. X-ray diffraction patterns of $(Fe_{50}Co_{50})_{62}Nb_8B_{30}$ heated up to: (a) crystallization peak and (b) 50 K below the melting temperature.

and T_p) it gives a measure for estimating the glass-forming ability to some extent. Namely, materials with smaller K_{cr} have a better GFA [9].

3.1. The crystallization products

Figs. 5 and 6 shows X-ray diffraction patterns of the Co containing alloys: (1) heated up to the first peak and (2) heated up to a temperature, which is about 50 K below the melting temperature. After the crystallization peak, we identify two phases, bcc Fe(Co) and the soft magnetic phase

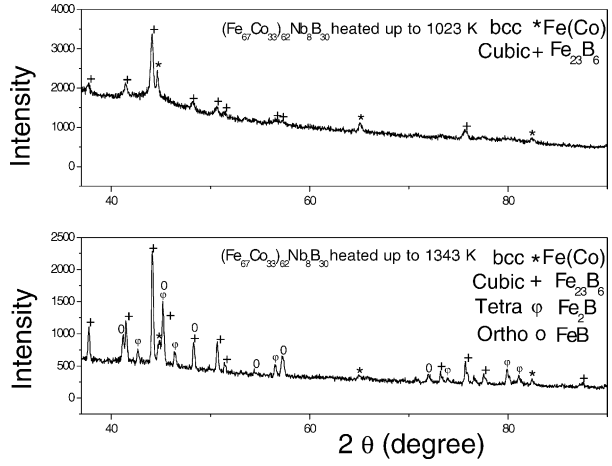

Fig. 5. X-ray diffraction patterns of $(Fe_{67}Co_{33})_{62}Nb_8B_{30}$ heated up to: (a) crystallization peak and (b) 50 K below the melting temperature.

cubic $Fe_{23}B_6$. Similar to the Co-free alloy, instead of the expected Fe_2B crystallization product, in the first crystallization step (at 1023 K) a rarely found $Fe_{23}B_6$ phase appears beside the bcc Fe(Co). Very probably, the Nb alloying element is responsible for the formation of the metastable $Fe_{23}B_6$ as it does in other Nb containing nanocrystalline alloys [10,11]. Fifty Kelvin before melting temperature, two additional phases appear: orthorhombic FeB and tetragonal Fe_2B.

The particle size by X-ray diffraction was determined by using Scherrer formula [12,13].

$$D = \frac{K\lambda}{B\cos\theta} \tag{3}$$

where D is the volume weight average grain size, B the full-width at half maximum (FWHM), K a constant, λ the wave length, and θ the Bragg angle.

The metastable phase of $Fe_{23}B_6$ was studied in more detail on the samples obtained after heating up to the first crystallization peak, considering only the Bragg peaks of 511 and 110 planes of $Fe_{23}B_6$ and Fe(Co), respectively (Fig. 7). With increasing Co concentration, the peaks are shifted to higher angle and become narrower. It follows that the grain size of $Fe_{23}B_6$ phase increases with Co concentration (Fig. 8) and its lattice constant decreases (inset of Fig. 8). This decrease of the lattice parameter is in line with the decrease of the lattice parameter of other Fe based phases, where Co substitutes the Fe atom [14].

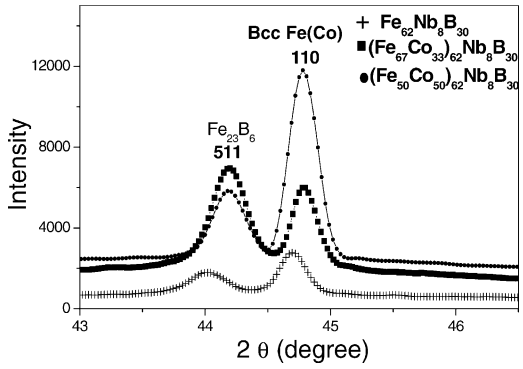

Fig. 7. The effect of Co addition on the Bragg peak position of bcc Fe(Co) and $Fe_{23}B_6$ of $(Fe_{100-x}Co_x)_{62}Nb_8B_{30}$ ($x = 0$, 33, and 50).

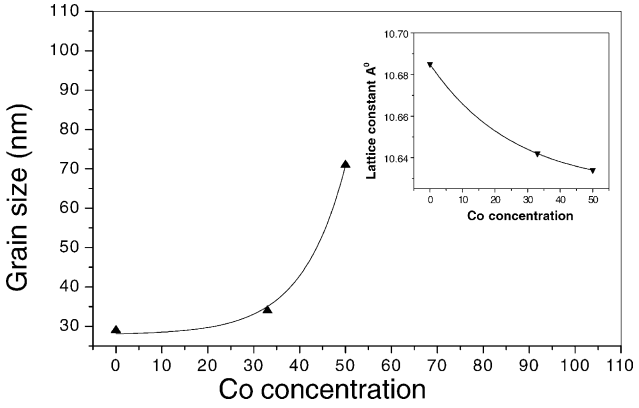

Fig. 8. The effect of Co addition on the grain size of $Fe_{23}B_6$. The inset shows the variation of the lattice constant of $Fe_{23}B_6$ phase with Co concentration.

4. Conclusions

We examined the effect of Co addition on the kinetics of crystallization process for $(Fe_{100-x}Co_x)_{62}Nb_8B_{30}$ ($x = 33$ and 50). Although T_g is shifted systematically to lower temperatures with increasing Co concentration the glass-forming ability expressed by ΔT_x shows a non-monotonic variation. A strong correlation was found between ΔT_x and $T_x/(T_g + T_l)$ and between ΔT_x and $T_x/(T_l - T_g)$. Nb induces the precipitation of the metastable $M_{23}B_6$ phase and stabilizes it up to the second crystallization stage. Co is divided between the two phases: bcc Fe(Co) and cubic $[Fe(Co)]_{23}B_6$ decreasing the lattice constant of both phases.

Acknowledgements

The Hungarian Scientific Research Fund supported this work through OTKA Grant No. T034 666 and T029701.

References

[1] T. Itoi, A. Inoue, Appl. Phys. Lett. 74 (1999) 2510.
[2] A. Inoue, Mater. Trans. JIM 40 (1999) 643.
[3] Z.P. Lu, C.T. Liu, Acta Mater. 50 (2002) 3051.
[4] A. Inoue, Bulk Amorphous Alloys, Preparation and Fundamental Characteristics, vol. 4, Trans Tech Publishers, 1998.
[5] K.Q. Qiu, H.F. Zhang, A.M. Wang, B.Z. Ding, Z.Q. Hu, Acta Mater. 50 (2002) 3567–3578.
[6] H.-G. Kim, J. yun park, S. Yamamuro, K. Sumiyama, K. Suzuki, Mater. Sci. Eng. A 217 (1996) 269.
[7] R. Bruning, K. Samwer, Phys. Rev. B 46 (1996) 11318.
[8] H.E. Kissinger, Anal. Chem. 29 (1957) 1702.
[9] N. Mitrovic, S. Roth, J. Eckert, Appl. Phys. 78 (2001) 2145.
[10] D.H. Ping, K. Hono, H. Kanekiyo, S. Hirosawa, Acta Mater. 47 (1999) 4641.
[11] J.S. Bla'zquez, C.F. Conde, A. Conde, Appl. Phys. Lett. 79 (2001) 2898.
[12] H.P. Klug, L.E. Alexander, X-ray Diffraction Procedures for Polycrstalline and Amorphous Materials, Wiley, New York, 1974.
[13] H. Natter, M. Schmelzer, M.S. Loffler, C.E. Krill, A. Fitch, R. Hempelmann, J. Phys. Chem. 104 (2000) 2467.
[14] S.G.E. te Velthuis, J.H. Root, M. Sietsma, Th. Rekveldt, S. Van der Zwaag, Acta Mater. 46 (1998) 5223.